UMT PRESS
Journal of Mathematical Sciences and Informatics
Journal Homepage: https://journal.umt.edu.my/index.php/jmsi
eISSN: 2948-3697
DOI: http://doi.org/10.46754/jmsi.2026.06.004

HEAT TRANSFER OPTIMISATION FOR ROTATING TERNARY HYBRID NANOFLUID WITH OPPOSING MIXED CONVECTION PAST A VERTICAL FLAT PLATE

NUR SYAHIRAH WAHID[1]*, RUSYA IRYANTI YAHAYA[2], NURUL IZZAH KHALID[3], MOHD SHAFIE MUSTAFA[1], NORIHAN MD ARIFIN[1,2], NAJIYAH SAFWA KHASHI'IE[4] AND IOAN POP[5,6]

[1]Department of Mathematics and Statistics, Faculty of Science, Universiti Putra Malaysia, 43400 Serdang, Selangor, Malaysia. [2]School of Quantitative Sciences, Universiti Utara Malaysia, 06010 Sintok, Kedah, Malaysia. [3]Department of Food Technology, Faculty of Food Science and Technology, Universiti Putra Malaysia, 43400 Serdang, Selangor, Malaysia. [4]Faculty of Mechanical Technology and Engineering, Universiti Teknikal Malaysia Melaka, Hang Tuah Jaya, 76100 Durian Tunggal, Melaka, Malaysia. [5]Department of Mathematics, Babeş-Bolyai University, R-400084 Cluj-Napoca, Romania. [6]Academy of Romanian Scientists, 3 Ilfov Street, 050044 Bucharest, Romania.

**Corresponding author: syahirahwahid@upm.edu.my*

ARTICLE INFO

Article History:
Received: 29 December 2025
Revised: 5 February 2026
Accepted: 9 April 2026
Published: 15 June 2026

Keywords:
Ternary hybrid nanofluid, mixed convection, rotating plate, response surface methodology.

ABSTRACT

The present study focuses on analysing and improving the heat - transfer performance of a rotating ternary hybrid nanofluid over a vertical flat surface under opposing mixed convection conditions. By employing suitable similarity transformations, the governing boundary-layer equations are reduced to nonlinear ordinary differential equations and subsequently solved using a MATLAB-based numerical approach. Furthermore, Response Surface Methodology (RSM) is used to investigate the combined influence of key parameters and to determine the conditions that maximise heat transfer efficiency. Increasing the concentration of nanoparticles, especially copper can greatly improve heat transfer efficiency, with copper nanoparticles showing the greatest enhancement, followed by aluminium oxide, (Al_2O3) and titanium dioxide (TiO_2) nanoparticles. Furthermore, desirability-based optimisation reveals that the heat-transfer rate attains a maximum value of 0.442152 with 99.93% desirability when the coded parameters A, B, and C (nanoparticle volume fractions) are at their maximum levels. Meanwhile, the decrement in skin friction along the x-direction is primarily influenced by the increase in volume fraction of copper nanoparticles, followed by titanium dioxide (TiO_2) and aluminium oxide nanoparticles. The findings provide significant insights into optimising heat-transfer in complex fluid dynamics systems, with potential applications in diverse industrial and engineering domains.

2020 Mathematics Subject Classification:

Introduction

A ternary hybrid nanofluid is an advanced form of nanofluid that consists of a suspension of three different types of nanoparticles, typically including metal oxides, carbon nanotubes, and non-metallic particles, dispersed within a base fluid. Compared to traditional nanofluids and hybrid nanofluids, it is generally acknowledged that ternary hybrid nanofluids exhibit enhanced heat transfer capabilities and thermal conductivity, which makes them potentially useful in various applications such as heat exchangers, nuclear reactor cooling, automotive cooling, and military applications. The shape and loading fraction of the nanoparticles, and the intrinsic properties of the base fluid, are crucial factors that affect the performance of ternary hybrid nanofluids.

Emerging studies indicate that numerical analyses of ternary hybrid nanofluid have escalated recently due to the recognised importance of its applications in thermal management. For instance, Khan *et al.* [1] scrutinised the time-dependent flow of ternary hybrid nanofluid over radially contracting or expanding, and rotating permeable sphere. The findings reveal that wall expansion leads to increased torque requirements accompanied by reduced drag.

Jan *et al.* [2] studied the ternary hybrid nanofluid flow over a stretching sheet under the influence of a magnetic field and convective boundary conditions using the Runge-Kutta method. Alharbi [3] analysed the heat transfer characteristics of the ternary hybrid nanofluid with slip and suction over a stretching or shrinking sheet. It was observed that, in the absence of suction and slip effects, the Nusselt number decreased in the shrinking case whereas the opposite behaviour was observed in the stretching case. Recently, Hussain *et al.* [4] modelled and solved the magnetohydrodynamic ternary hybrid nanofluid flow over a stretching sheet with convective boundary conditions. They considered graphene oxide, silver, and copper as the ternary nanoparticles with kerosene acting as the base fluid. A review of ternary hybrid nanofluids in the context of thermophysical properties, synthesis, stability, applications, and environmental effects was conducted by Adun *et al.* [5]. Also, several other studies on ternary hybrid nanofluid can be found in the following literature: [6–10].

Opposing flow in mixed convection arises when the fluid is forced to move in the opposite direction to the rising fluid due to thermal buoyancy effects. This phenomenon is significant in various engineering applications, including heat exchangers, solar collectors, and microelectronic cooling systems. In the context of boundary-layer flow of ternary hybrid nanofluid, the incorporation of mixed convection into the mathematical modelling remains limited d in the literature which motivates the emergence of present study. Anyhow, the available study of ternary hybrid nanofluid flow with mixed convection was conducted by Jamrus *et al.* [11] with also the consideration of magnetohydrodynamic and thermal stratification. Moreover, the study of rotating flow past a vertical plate involves analysing the characteristics of the flow field and its influence on boundary-layer dynamics. Research on this topic delves into the effects of rotation on fluid behaviour, particularly in the context of boundary layer flow past a vertical surface.

The interaction between the rotating fluid and the stationary plate leads to complex flow patterns and boundary-layer development. Various parameters such as rotational speed, fluid properties, and plate geometry influence the flow structure and heat transfer characteristics in this configuration. It seems the study on rotating flow of ternary hybrid nanofluid is also still

limited but in the context of only hybrid nanofluid, several studies have been found in the literature. For example, the rotating flow of hybrid nanofluid with radiation over a shrink surface with heat generation or absorption has been studied by Yasir *et al.* [12]. The boost in rotation parameter has enhanced the shear stresses by approximately 5.29% for one of the solutions. Considering three-dimensional configuration, Asghar *et al.* [13] also studied the rotating flow of hybrid nanofluid and concluded that the rotation parameter enhanced the velocity profile of the flow. Further, Kodi *et al.* [14] also studied the three-dimensional rotating hybrid nanofluid flow with hall current for the flow over stretching plate, while most recently, Mohana Ramana *et al.* [15] also studied the rotating flow of the hybrid nanofluid with porosity effect.

The main goal of this study is to examine the behaviour of rotating ternary hybrid nanofluid flow with opposing mixed convection past a vertical flat plate in a three-dimensional space. The focus is on understanding the intricate dynamics of fluid-flow and heat-transfer in this complex system. To achieve this, a numerical method will be employed to solve the model and simulate the physical phenomena. Additionally, the statistical method known as Response Surface Methodology (RSM) is utilised to analyse and optimise the effects of various parameters on the system's performance. Software tools such as MATLAB, Minitab, and Design Expert are used to facilitate the computational and statistical processes. This combined approach will provide comprehensive insights into the fluid-flow and heat transfer of ternary hybrid nanofluids under rotating conditions.

Mathematical Model

Let us consider the three-dimensional (3D) mixed convection ternary hybrid nanofluid flow past a rotating vertical plate on the (x, y) plane (Figure 1), where (x, y, z) are Cartesian coordinates with z–axis measured in the vertical direction, the flow occupies the domain $z \geq 0$. The plate is assumed to rotate around z–axis with the constant velocity Ω_0. The variable temperatures of the plate is $T_w(x, y) = T_\infty + T_0(x + y)/l$, where T_0 is flow characteristic with $T_0 > 0$ for the assisting flow, $T_0 < 0$ for opposing flow, and $T_0 = 0$ is for forced convection flow, T_∞ is the constant ambient temperature, and l is the characteristic length of the plate.

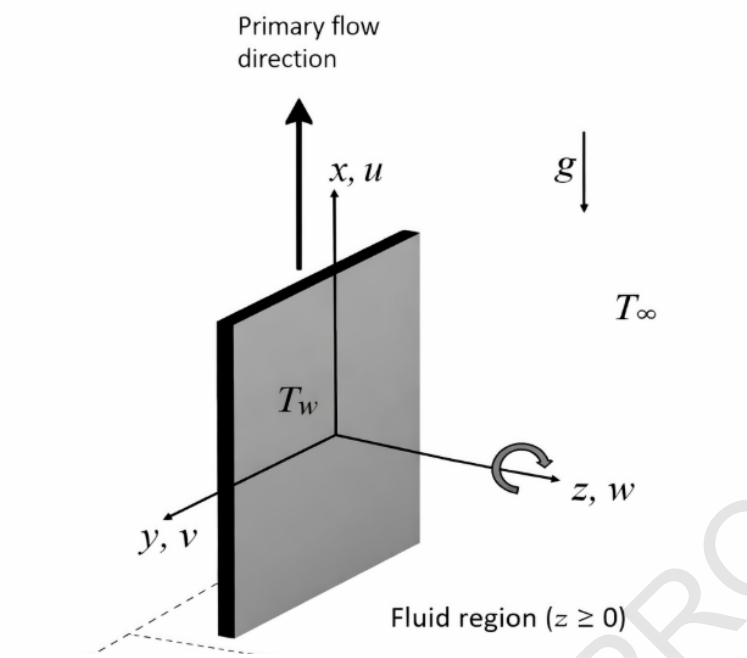

Figure 1: Physical model for 3D vertical flat plate

Under above assumptions, the model of boundary -layer flow can be formulated as [16-18]:

$$\frac{\partial u}{\partial x}+\frac{\partial v}{\partial y}+\frac{\partial w}{\partial z}=0, \tag{1}$$

$$u\frac{\partial u}{\partial x}+v\frac{\partial u}{\partial y}+w\frac{\partial u}{\partial z}-2\Omega_0 v=\frac{\mu_{thnf}}{\rho_{thnf}}\frac{\partial^2 u}{\partial z^2}+\beta_{thnf}\left(T-T_\infty\right)g^*, \tag{2}$$

$$u\frac{\partial v}{\partial x}+v\frac{\partial v}{\partial y}+w\frac{\partial v}{\partial z}+2\Omega_0 u=\frac{\mu_{thnf}}{\rho_{thnf}}\frac{\partial^2 v}{\partial z^2}, \tag{3}$$

$$u\frac{\partial T}{\partial x}+v\frac{\partial T}{\partial y}+w\frac{\partial T}{\partial z}=\frac{k_{thnf}}{\left(\rho C_p\right)_{thnf}}\frac{\partial^2 T}{\partial z^2}, \tag{4}$$

subject to:

$$\left.\begin{array}{l}\left.\begin{array}{l}u=u_w\left(x,y\right)=0,\ v=v_w\left(x,y\right)=0,\ w=0,\\ T=T_w\left(x,y\right)=T_\infty+\dfrac{T_0\left(x+y\right)}{l},\end{array}\right\}\ \text{at } z=0,\\ u\to 0,\ v\to 0,\ T\to T_\infty\ \text{as } z\to\infty.\end{array}\right\} \tag{5}$$

Here, $\left(u,v,w\right)$ symbolised the velocity of the fluid-flow model along $\left(x,y,z\right)$–axis, T is the temperature of the fluid, g^* is gravitation velocity and a is a positive constant. The model of the physical properties of the ternary hybrid nanofluids is given in Table 1 and the respective properties of water (H_2O), alumina (Al_2O_3) (first nanoparticle), copper (Cu) (second nanoparticle), and titanium dioxide (TiO_2) (third nanoparticle) are given in Table 2. It should be noted that the subscript of *thnf* refer to ternary hybrid nanofluid, *hnf* refer to hybrid

nanofluid, *mph* refers to nanofluid and *f* refers to the base fluid, while the subscript of 1, 2, and 3 refers to the first, second, and third nanoparticles respectively.

Table 1: Thermophysical properties model [19]

Properties	Model Correlation
Dynamic viscosity	$\mu_{thnf} = \dfrac{\mu_f}{(1-\phi_1)^{2.5}(1-\phi_2)^{2.5}(1-\phi_3)^{2.5}}$
Density	$\rho_{thnf} = (1-\phi_1)\left\{(1-\phi_2)\left[(1-\phi_3)\rho_f + \phi_3\rho_3\right] + \phi_2\rho_2\right\} + \phi_1\rho_1$
Heat capacitance	$(\rho C_p)_{thnf} = (1-\phi_1)\left\{(1-\phi_2)\left[(1-\phi_3)(\rho C_p)_f + \phi_3(\rho C_p)_3\right] + \phi_2(\rho C_p)_2\right\} + \phi_1(\rho C_p)_1$
Thermal conductivity	$k_{thnf} = \dfrac{k_1 + 2k_{hnf} - 2\phi_1(k_{hnf} - k_1)}{k_1 + 2k_{hnf} + \phi_1(k_{hnf} - k_1)} \times k_{hnf}$ where $k_{hnf} = \dfrac{k_2 + 2k_{nf} - 2\phi_2(k_{nf} - k_2)}{k_2 + 2k_{nf} + \phi_2(k_{nf} - k_2)} \times k_{nf}$ and $k_{nf} = \dfrac{k_3 + 2k_f - 2\phi_3(k_f - k_3)}{k_3 + 2k_f + \phi_3(k_f - k_3)} \times k_f$
Thermal expansion	$\beta_{thnf} = (1-\phi_1)\left\{(1-\phi_2)\left[(1-\phi_3)\beta_f + \phi_3\beta_3\right] + \phi_2\beta_2\right\} + \phi_1\beta_1$

Table 2: Thermophysical properties value [20, 21]

Properties	Water	Alumina (1st)	Copper (2nd)	Titanium Dioxide (3rd)
$\rho(\mathrm{kg/m^3})$	997.1	3,970	8,933	4,250
$C_p\,(\mathrm{J/kgK})$	4,179	765	385	686.2
$k(\mathrm{W/mK})$	0.613	40	400	8.9538
$\beta(1/K)$	21×10^{-5}	0.85×10^{-5}	1.67×10^{-5}	0.9×10^{-5}
Pr	6.2	NA	NA	NA

Invoking the following similarity variables [17]:

$$\left.\begin{aligned} &u = a(x+y)f'(\eta),\ v = a(x+y)g'(\eta),\ w = -\sqrt{av_f}\left[f(\eta)+g(\eta)\right], \\ &\theta(\eta) = \frac{T-T_\infty}{T_w-T_\infty},\ \eta = z\sqrt{\frac{a}{v_f}}, \end{aligned}\right\} \tag{6}$$

Equation (1) is satisfied, and Equations (2), (3), and (4) are simplified into the following:

$$\left(\frac{\mu_{thnf}/\mu_f}{\rho_{thnf}/\mu_f}\right)f'''+(f+g)f''-(f'+g')f'+2\Omega g'+\frac{\beta_{thnf}}{\beta_f}\lambda\theta=0, \tag{7}$$

$$\left(\frac{\mu_{thnf}/\mu_f}{\rho_{thnf}/\mu_f}\right)g'''+(f+g)g''-(f'+g')g'-2\Omega f'=0, \tag{8}$$

$$\frac{1}{\Pr}\frac{k_{thnf}/k_f}{\left(\rho C_p\right)_{thnf}/\left(\rho C_p\right)_f}\theta''+(f+g)\theta'-(f'+g')\theta=0, \tag{9}$$

subject to:

$$\begin{aligned} &f(\eta)=g(\eta)=0,\ f'(\eta)=g'(\eta)=0,\ \theta(\eta)=1 \text{ at } \eta=0,\\ &f'(\eta)\to 0,\ g'(\eta)\to 0,\ \theta(\eta)\to 0 \text{ as } \eta\to\infty. \end{aligned} \tag{10}$$

such that the related parameters can be defined as:

$$\begin{aligned} &\text{Prandtl number} = \Pr=\frac{v_f\left(\rho C_p\right)_f}{k_f},\\ &\text{Dimensionless rotation parameter} = \Omega=\frac{\Omega_0}{a},\\ &\text{Mixed convection parameter} = \lambda=\frac{Gr_x}{\mathrm{Re}_x^2}, \end{aligned} \tag{11}$$

where $Gr_x=g^*\beta_f\left(T_w-T_\infty\right)(x+y)^3/v_f^2$ is the local Grashof number and $\mathrm{Re}_x=u_e(x,y)(x+y)/v_f$ is the local Reynolds number. Noted that $\lambda>0$ corresponds to the assisting flow, $\lambda<0$ is for opposing flow and $\lambda=0$ corresponds to the forced convection flow, respectively. However, for the present study, we only focus on the opposing type of mixed convection flow.

The physical quantities of interest are the skin friction coefficients (C_{fx} and C_{fy}) and the local Nusselt number Nu_x, such that [17]:

$$C_{fx}=\frac{\mu_{thnf}}{\rho_f u_e^2}\left(\frac{\partial u}{\partial z}\right)_{z=0},\ C_{fy}=\frac{\mu_{thnf}}{\rho_f v_e^2}\left(\frac{\partial v}{\partial z}\right)_{z=0},\ Nu_x=-\frac{(x+y)k_{thnf}}{k_f\left(T_w-T_\infty\right)}\left(\frac{\partial T}{\partial z}\right)_{z=0}. \tag{12}$$

After transformation, we have:

$$\mathrm{Re}_x^{1/2}C_{fx}=\frac{\mu_{thnf}}{\mu_f}f''(0),\ \mathrm{Re}_y^{1/2}C_{fy}=\frac{\mu_{thnf}}{\mu_f}g''(0),\ \mathrm{Re}_x^{-1/2}Nu_x=-\frac{k_{thnf}}{k_f}\theta'(0). \tag{13}$$

where $\mathrm{Re}_x=\frac{u_e(x+y)}{v_f}$ and $\mathrm{Re}_y=\frac{v_e(x+y)}{v_f}$ are the local Reynolds numbers, respectively.

Results and Discussion

To analyse the fluid-flow model, Equations (7) to (9), together with Equation (10), are solved numerically. Prior to generating the solutions, a comprehensive code validation is performed by comparing the results obtained from our b*vp4c* implementation with those reported in previous studies. Table 3 demonstrates excellent agreement between our numerical outcomes and the published data, thereby confirming the accuracy the developed model and computational approach. This rigorous validation ensures the credibility of the subsequent numerical results and analyses.

Table 3: Comparison value for particular case when $f'(0)=1$ and $\lambda=\Omega=\phi_1=\phi_2=\phi_3=0$

Pr	$f''(0)$		$g''(0)$		$-\theta'(0)$	
	Present	**[17]**	**Present**	**[17]**	**Present**	**[17]**
0.7	-1	-1	0	0	0.793668	0.793668
1	-1	-1	0	0	1.000000	1.000000
7	-1	-1	0	0	3.072250	3.072250

Figures 2-4 illustrate $f'(\eta)$, $g'(\eta)$, and $\theta(\eta)$ for different values of λ when $\Omega=0.8$ and $\phi_1=\phi_2=\phi_3=1\%$. Notably, these distributions of $f'(\eta)$, $g'(\eta)$, and $\theta(\eta)$ exhibit inflection points, resulting in non-uniform behaviour. As the magnitude of λ increases, the velocity profile along the $x-$axis ($f'(\eta)$) decreases within the approximate range of $0<\eta<3$ but subsequently increases for $\eta>3$ before converging to 0. An opposite trend is observed for the velocity profile along the $y-$axis ($g'(\eta)$), with the inflection point occurring around $\eta=4$. Similarly, the temperature profile ($\theta(\eta)$) exhibits an increasing trend in some regions near the plate for $0<\eta<1.5$, but a decreasing trend is noted for $\eta>1.5$ as the magnitude of λ increases.

The distribution of $f'(\eta)$, $g'(\eta)$, and $\theta(\eta)$ with varying values of Ω when $\lambda=-1$ and $\phi_1=\phi_2=\phi_3=1\%$ are presented in Figures 5 to 7. As Ω increases, $f'(\eta)$ initially experiences an ascent within the approximate range of $0<\eta<3$, followed by a subsequent decline for $\eta>3$, ultimately approaching zero. Conversely, $g'(\eta)$ demonstrates an opposing trend, with an inflection point around $\eta=5$. For $\theta(\eta)$, an increase in Ω leads to a declining trend for $0<\eta<2.5$, while an increasing trend emerges for $\eta>2.5$. Physically, increasing the rotation parameter will accelerate fluid motion and complicate the boundary-layer formation [22]. Hence, the boundary-layer becomes thinner, as observed in Figures 5 to 7.

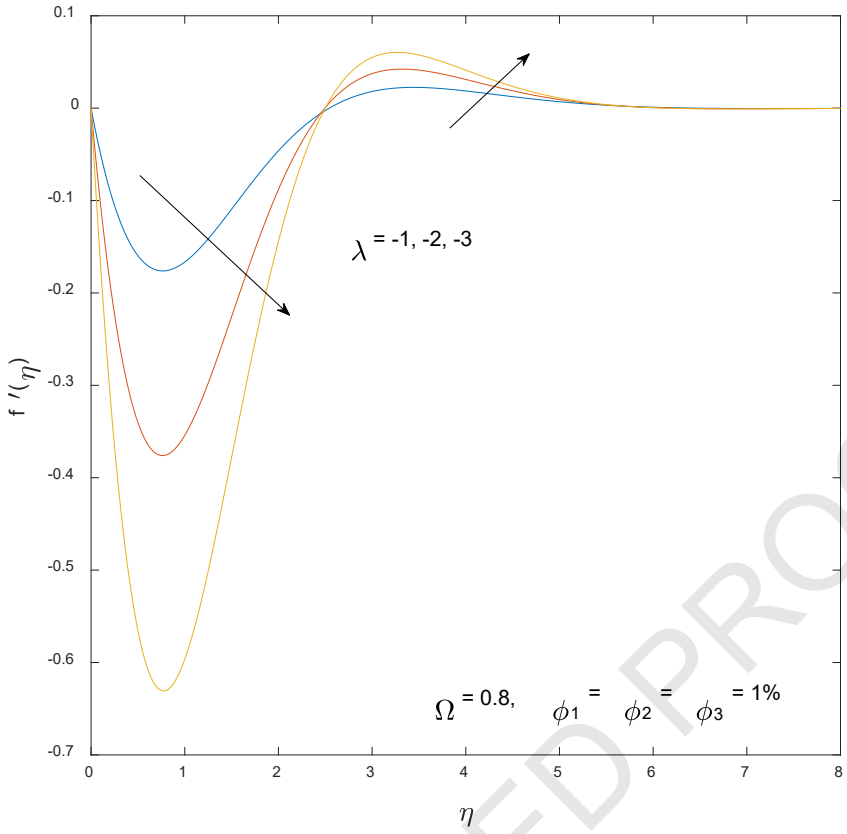

Figure 2: Distribution of $f'(\eta)$ for selected λ

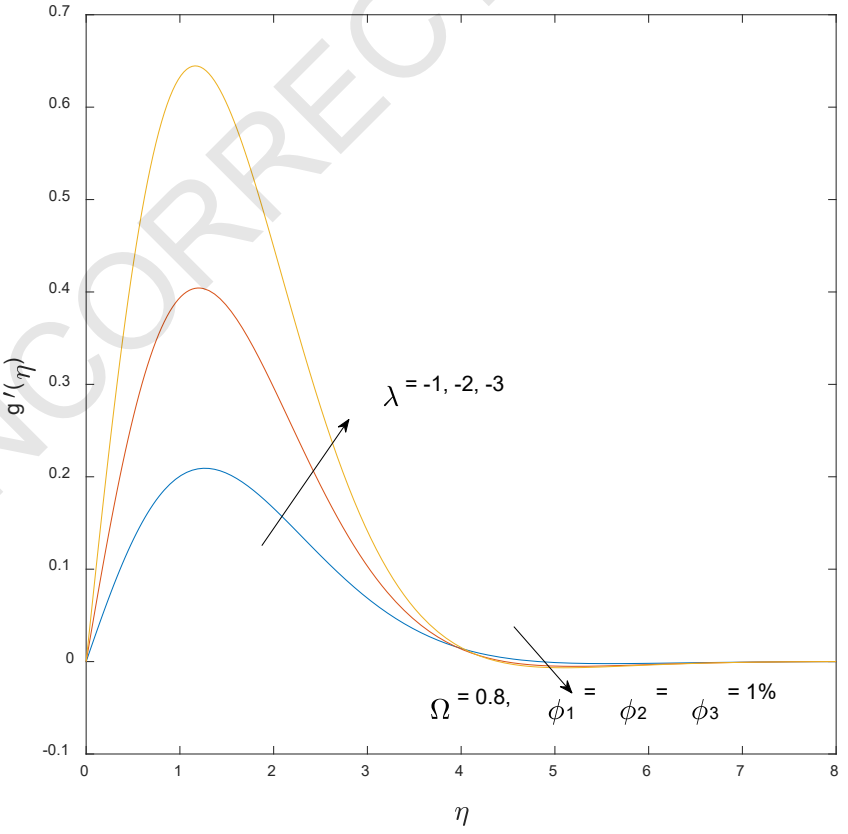

Figure 3: Distribution of $g'(\eta)$ for selected λ

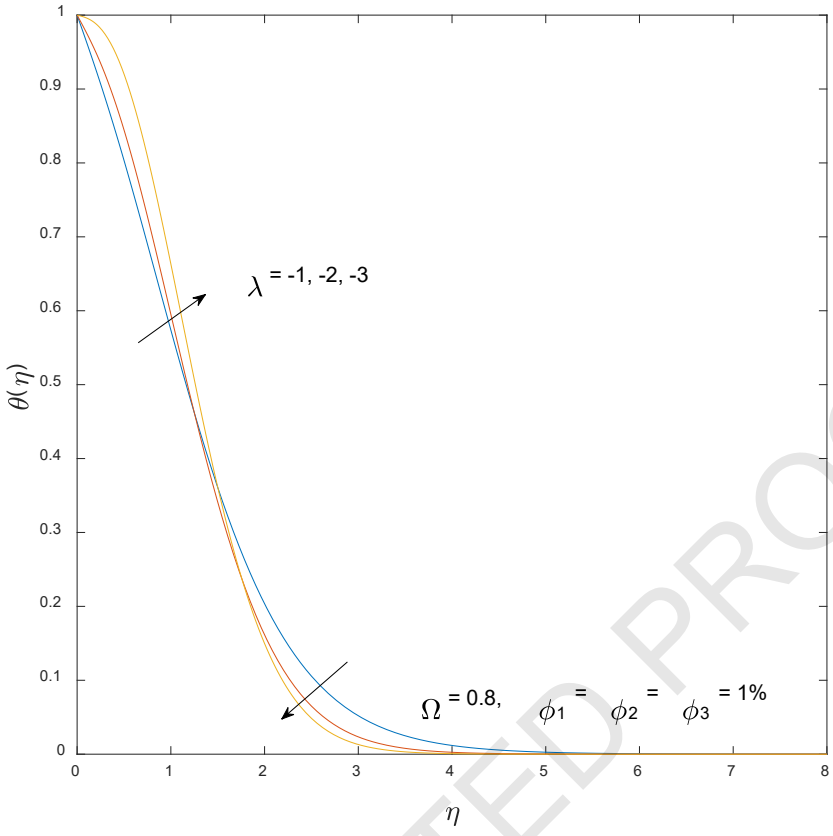

Figure 4: Distribution of $\theta(\eta)$ for selected λ

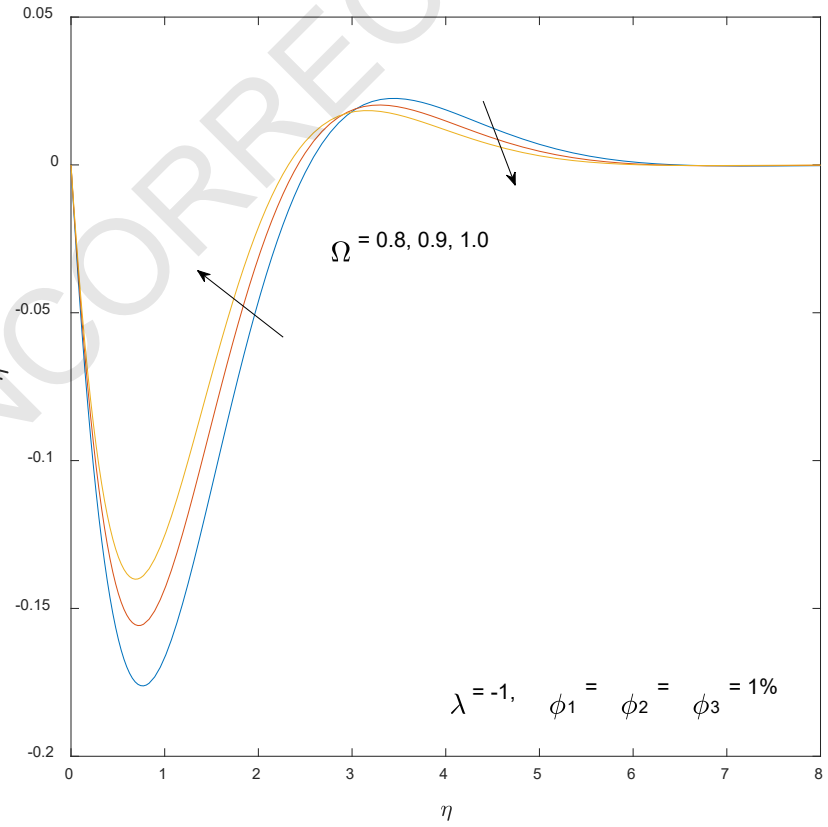

Figure 5: Distribution of $f'(\eta)$ for selected Ω

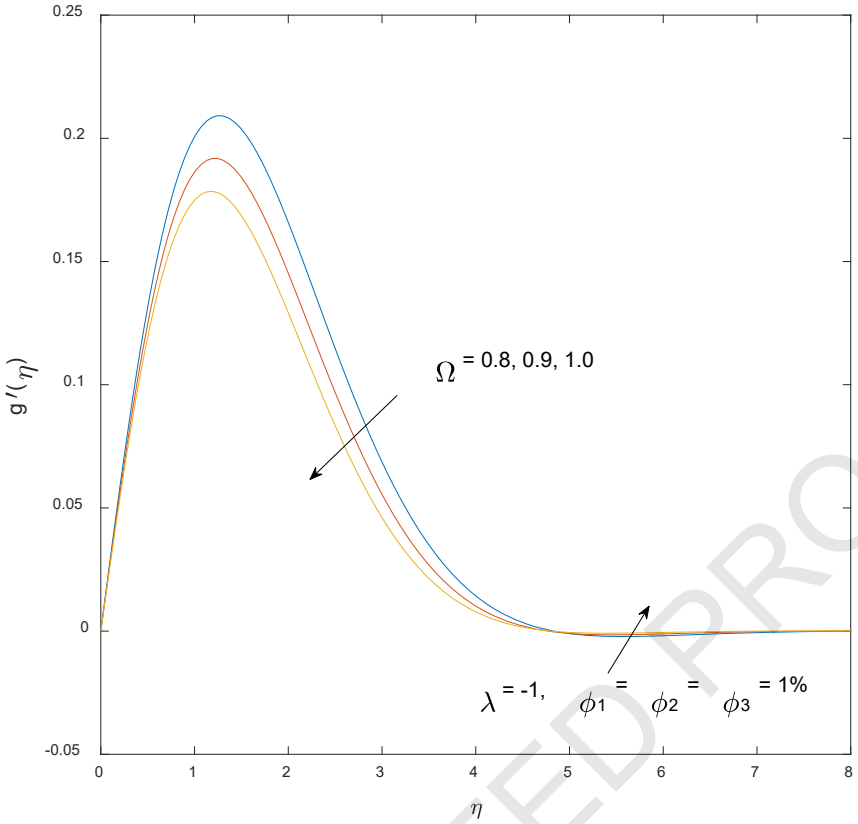

Figure 6: Distribution of $g'(\eta)$ for selected Ω

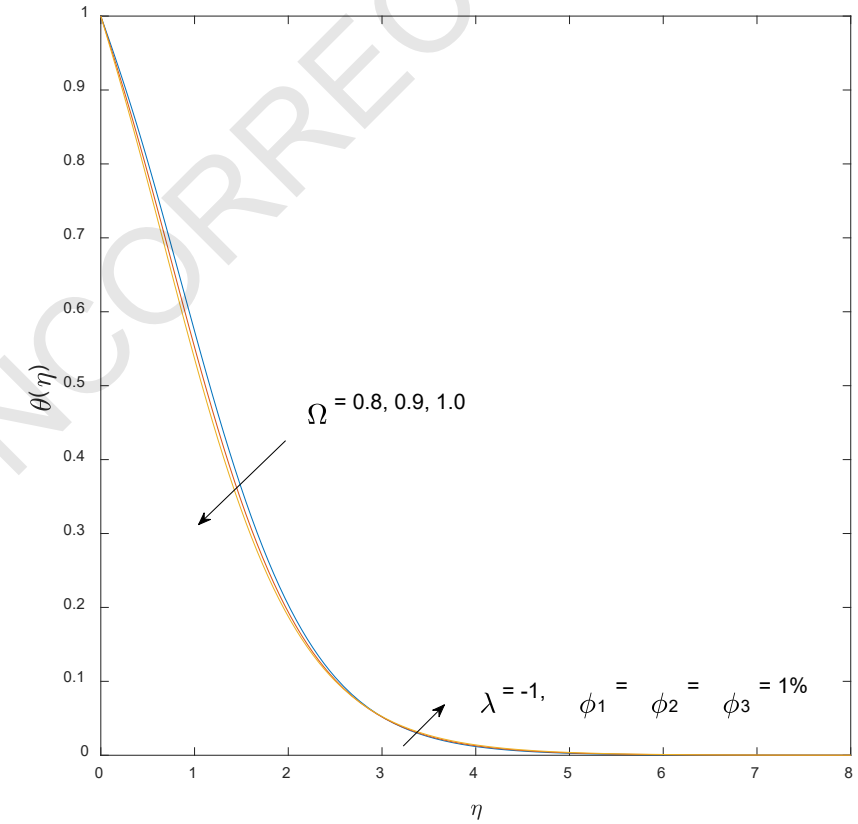

Figure 7: Distribution of $\theta(\eta)$ for selected Ω

The impact of λ and Ω on $\mathrm{Re}_x^{1/2} C_{fx}$, $\mathrm{Re}_y^{1/2} C_{fy}$, and $\mathrm{Re}_x^{-1/2} Nu_x$ is tabulated in Table 4 for the case of ternary hybrid nanofluid with constant volume fraction of nanoparticles such that $\phi_1 = \phi_2 = \phi_3 = 1\%$. It can be analysed that the increase in magnitude of λ causes $\mathrm{Re}_x^{1/2} C_{fx}$ and $\mathrm{Re}_x^{-1/2} Nu_x$ to reduce but in the opposite manner for $\mathrm{Re}_y^{1/2} C_{fy}$. Meanwhile, the increase of Ω causes $\mathrm{Re}_x^{1/2} C_{fx}$ and $\mathrm{Re}_x^{-1/2} Nu_x$ to increase but works in reverse $\mathrm{Re}_y^{1/2} C_{fy}$. In real-world applications, such as thermal management systems in electronics or industrial processes involving fluid-flow and heat-transfer, understanding the implications of these findings is crucial. For instance, in electronics cooling, where efficient heat dissipation is essential, the reduction in $\mathrm{Re}_x^{1/2} C_{fx}$ due to opposing mixed convection could lead to improved airflow and heat-transfer over the heat-generating components. However, the decrease in $\mathrm{Re}_x^{-1/2} Nu_x$ might necessitate adjustments to ensure adequate cooling performance. Similarly, optimising parameters like rotation can enhance heat-transfer in industrial processes while minimising energy consumption.

Table 4: Value of physical quantities of interest for different λ and Ω for the ternary hybrid nanofluid

λ	Ω	$\mathrm{Re}_x^{1/2} C_{fx}$	$\mathrm{Re}_y^{1/2} C_{fy}$	$\mathrm{Re}_x^{-1/2} Nu_x$
-1	0.8	-0.583207842	0.315770451	0.391672195
	0.9	-0.546844814	0.302194768	0.431356876
	1	-0.517503263	0.291824361	0.461098249
-2	0.8	-1.222293253	0.637307614	0.255039245
	0.9	-1.126056546	0.591727645	0.342613696
	1	-1.053850199	0.560365678	0.405501712
-3	0.8	-1.974429314	1.037331742	0.033916189
	0.9	-1.770906409	0.922590987	0.194555220
	1	-1.632094106	0.851709776	0.300828593

To further assess the impact of nanoparticle volume fractions of each constituent in the ternary hybrid nanofluid on the skin friction and heat transfer rate, the RSM is employed. This method utilises the data presented in Table 5, acquired from the numerical solver, with $\mathrm{Re}_x^{-1/2} Nu_x$ representing the heat transfer rate. Specifically, the volume fractions of alumina, copper, and titanium dioxide nanoparticles are denoted as the independent parameters, while $\mathrm{Re}_x^{1/2} C_{fx}$, $\mathrm{Re}_y^{1/2} C_{fy}$, and $\mathrm{Re}_x^{-1/2} Nu_x$ are the response. The independent parameters are considered at three distinct levels for each component, with their coded symbols and respective levels tabulated in Table 6. Then, the relationship between the independent parameters and response is given by the following second-order equation [23,24]:

$$\begin{aligned}\text{Response} = {} & c_0 + c_1\mathrm{A} + c_2\mathrm{B} + c_3\mathrm{C} + c_1c_1\mathrm{AA} + c_2c_2\mathrm{BB} + c_3c_3\mathrm{CC} + c_1c_2\mathrm{AB} \\ & + c_1c_3\mathrm{AC} + c_2c_3\mathrm{BC}\end{aligned} \tag{14}$$

with the coefficients c to be determined through the RSM and the response $\mathrm{Re}_x^{1/2} C_{fx}$, $\mathrm{Re}_y^{1/2} C_{fy}$, and $\mathrm{Re}_x^{-1/2} Nu_x$ are written as SFX, SFY, and HT, respectively.

Table 5: Value of physical quantities of interest for different volume fraction of nanoparticles when $\lambda = -1$ and $\Omega = 0.8$

Runs	ϕ_1	ϕ_2	ϕ_3	$\mathrm{Re}_x^{1/2} C_{fx}$	$\mathrm{Re}_y^{1/2} C_{fy}$	$\mathrm{Re}_x^{-1/2} Nu_x$
1	0	0	0	-0.542654995	0.289725497	0.337514656
2	0.02	0	0	-0.560871137	0.301542920	0.366547197
3	0	0.02	0	-0.586577690	0.317705493	0.390486933
4	0.02	0.02	0	-0.603704561	0.329167265	0.417608592
5	0	0	0.02	-0.562399157	0.302310492	0.364413659
6	0.02	0	0.02	-0.580242007	0.314055480	0.392661421
7	0	0.02	0.02	-0.605605695	0.330167488	0.415540056
8	0.02	0.02	0.02	-0.622411938	0.341558915	0.442222882
9	0	0.01	0.01	-0.574478106	0.309988330	0.377750638
10	0.02	0.01	0.01	-0.591958810	0.321592012	0.405411597
11	0.01	0	0.01	-0.561533679	0.301872723	0.365539656
12	0.01	0.02	0.01	-0.604559530	0.329617125	0.416652605
13	0.01	0.01	0	-0.573609648	0.309540368	0.378764805
14	0.01	0.01	0.02	-0.592808298	0.322028849	0.404329958
15						
16						
17		0.01		-0.583207842	0.315770451	0.391672195
18						
19						
20						

Table 6: Parameter and level

Parameter	**Coded parameter**	**Level**		
		-1 (minimum)	**0 (medium)**	**1 (maximum)**
ϕ_1	A			
ϕ_2	B	0	0.01	0.02
ϕ_3	C			

A face-centred central composite design (FCD) consisting of 20 runs is employed for the RSM. The objective is to determine the optimal composition, by examining various nanoparticle volume fractions, which minimise or maximise skin friction while simultaneously maximising the heat transfer rate. This approach aims to facilitate the efficient performance of practical applications that demand lower or higher skin friction while achieving enhanced heat

transfer capabilities. Thereby optimising the overall system's thermal and hydrodynamic characteristics.

Tables 7-9 present the analysis of variance (ANOVA) based on the numerical data in Table 5. Accordingly, the regression Equations (15)- (17) are obtained. The *p*-values derived from the ANOVA, being less than 0.05, indicates that all terms in Equations 15-17 are statistically significant and the regression models are reliable. It can be expressed as follows:

$$\begin{aligned} SFX = &-0.583208 - 0.008747\,A - 0.021516\,B - 0.009605\,C - 0.000011\,AA \\ &+ 0.000161\,BB + 0.000266\,AB + 0.000087\,AC + 0.000172\,BC \end{aligned} \tag{15}$$

$$\begin{aligned} SFY = &\ 0.315770 + 0.005802\,A + 0.013871\,B + 0.006244\,C + 0.000020\,AA \\ &- 0.000025\,BB + 0.000014\,CC - 0.000089\,AB - 0.000018\,AC - 0.000030\,BC \end{aligned} \tag{16}$$

$$\begin{aligned} HT = &\ 0.391673 + 0.013875\,A + 0.025583\,B + 0.012825\,C - 0.000093\,AA \\ &- 0.000578\,BB - 0.000127\,CC - 0.000434\,AB - 0.000153\,AC - 0.000418\,BC \end{aligned} \tag{17}$$

Table 7: ANOVA for SFX

Source	DF	Adj SS	Adj MS	F-Value	*p*-Values
Model	8	0.006318	0.000790	15253853.16	
Linear	3	0.006317	0.002106	40670617.80	
A	1	0.000765	0.000765	14778720.27	0.000
B	1	0.004629	0.004629	89414394.94	
C	1	0.000923	0.000923	17818738.18	
Square	2			1151.23	
AA	1	0.000000		7.56	0.019
BB	1			1597.94	
2-way interaction	3	0.000001	0.000000	5556.48	
AB	1	0.000001		10911.32	0.000
AC	1			1162.57	
BC	1			4595.56	
Error	11	0.000000			
Lack-of-fit	6			*	*
Pure error	5				
Total	**19**	**0.006318**			

Table 8: ANOVA for SFY

Source	DF	Adj SS	Adj MS	F-Value	*p*-Values
Model	9	0.002651	0.000295	5.96516E+08	
Linear	3	0.002651	0.000884	1.78950E+09	
A	1	0.000337	0.000337	6.81814E+08	
B	1	0.001924	0.001924	3.89701E+09	
C	1	0.000390	0.000390	7.89665E+08	
Square	3			1835.02	
AA	1			2197.49	0.000
BB	1			3589.11	
CC	1			1139.03	
2-Way interaction	3			49189.71	
AB	1	0.000000		127345.48	
AC	1			5161.38	
BC	1			15062.28	
Error	10				
Lack-of-fit	5			*	*
Pure error	5				
Total	**19**	**0.002651**			

Table 9: ANOVA for HT

Source	DF	Adj SS	Adj MS	F-Value	*p*-Values
Model	9	0.010121	0.001125	431424.51	
Linear	3	0.010115	0.003372	1293541.17	
A	1	0.001925	0.001925	738551.52	0.000
B	1	0.006545	0.006545	2511074.42	
C	1	0.001645	0.001645	630997.58	
Square	3	0.000003	0.000001	336.34	
AA	1	0.000000		9.16	0.013
BB	1	0.000001		352.69	0.000
CC	1	0.000000		17.00	0.002
2-way interaction	3	0.000003	0.000001	396.01	
AB	1	0.000002		579.38	0.000
AC	1	0.000000		71.80	
BC	1	0.000001		536.85	
Error	10				
Lack-of-fit	5	0.000000		*	*
Pure error	5				
Total	**19**	**0.010121**			

Meanwhile, the interactions between the parameters and their effects on the response can be analysed from the surface and contour plots shown in Figures 8 - 10. Figure 8 presents the interactive effects of A, B, and C on the skin friction in the x-direction (SFX). The increase of A and B reduces SFX, with the increase in B producing a more pronounced reduction [Figure 8a]. It can also be observed from Figure 8b that C produces a more significant decrement towards SFX when interacting with A. Nevertheless, the effects of C on SFX become less pronounced when interacting with B. As seen from Figure 8 (c), the increase in B and C reduces SFX, but B produces a wider range of reductions. Hence, SFX is most strongly influenced by B, followed by C and A. Therefore, the reduction of skin friction in x-direction is mainly influenced by the increase of nanoparticle volume fraction of Cu, followed by TiO_2 and Al_2O_3 nanoparticles.

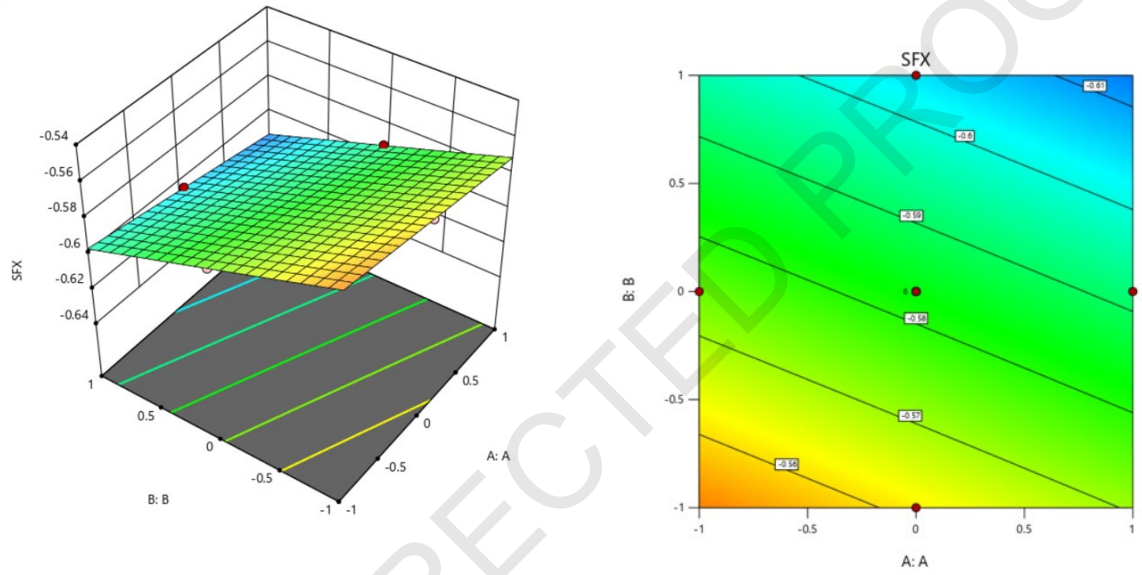

Figure 8 (a): Plots of A and B with response (skin friction in the x-direction)

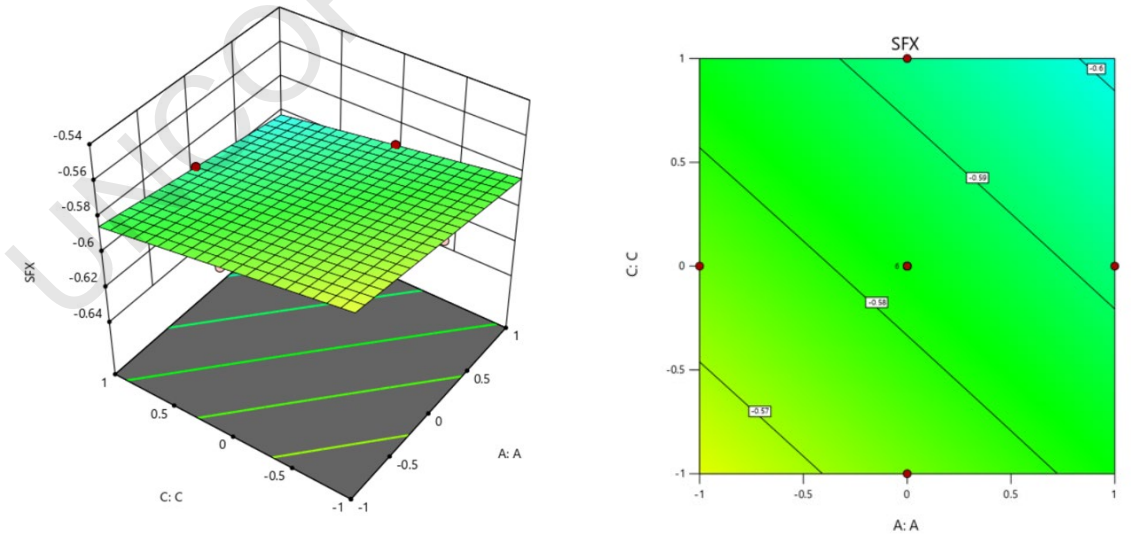

Figure 8 (b): Plots of A and C with response (skin friction in the x-direction)

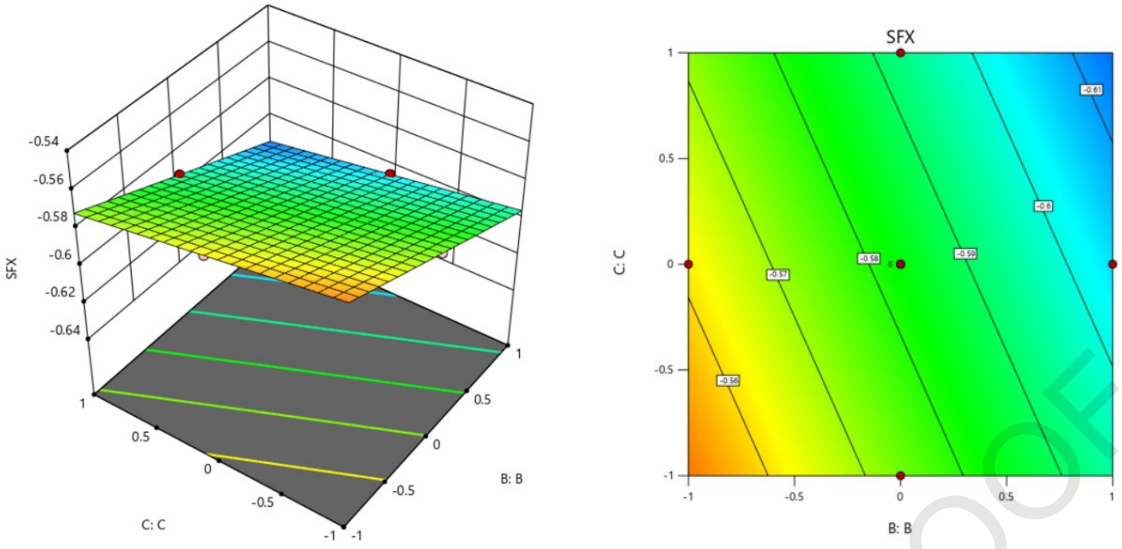

Figure 8 (c): Plots of C and B with response (skin friction in the *x*-direction)

Then, Figure 9 depicts the interactive impacts of independent parameters on the skin friction in *y*-direction (SFY). In contrast with SFX, the increase of *A, B*, and *C* enhances SFY. In Figures 9a and 9b, *B* and *C* are noted to have a more significant impact on improving SFY than *A*. However, it can be observed from Figure 9c that a more significant increase of SFY is achieved with *B* compared to *C*. Therefore, the increase of skin friction in *y*-direction is more influenced by the increase in nanoparticle volume fraction of Cu, followed by the TiO_2 and Al_2O_3 nanoparticles.

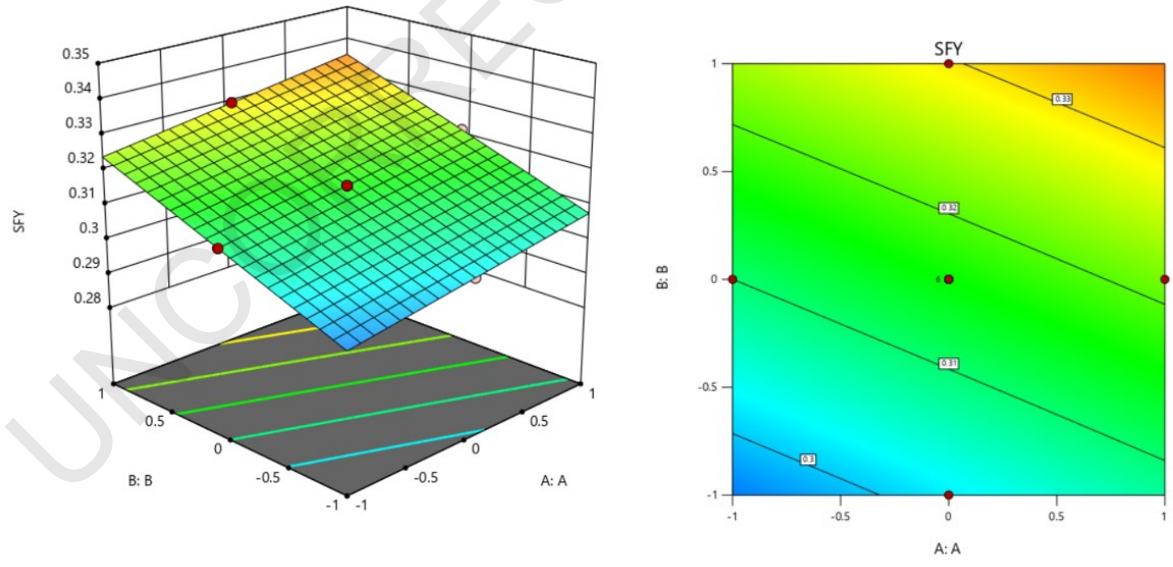

Figure 9 (a): Plots of A and B with response (skin friction in *y*-direction)

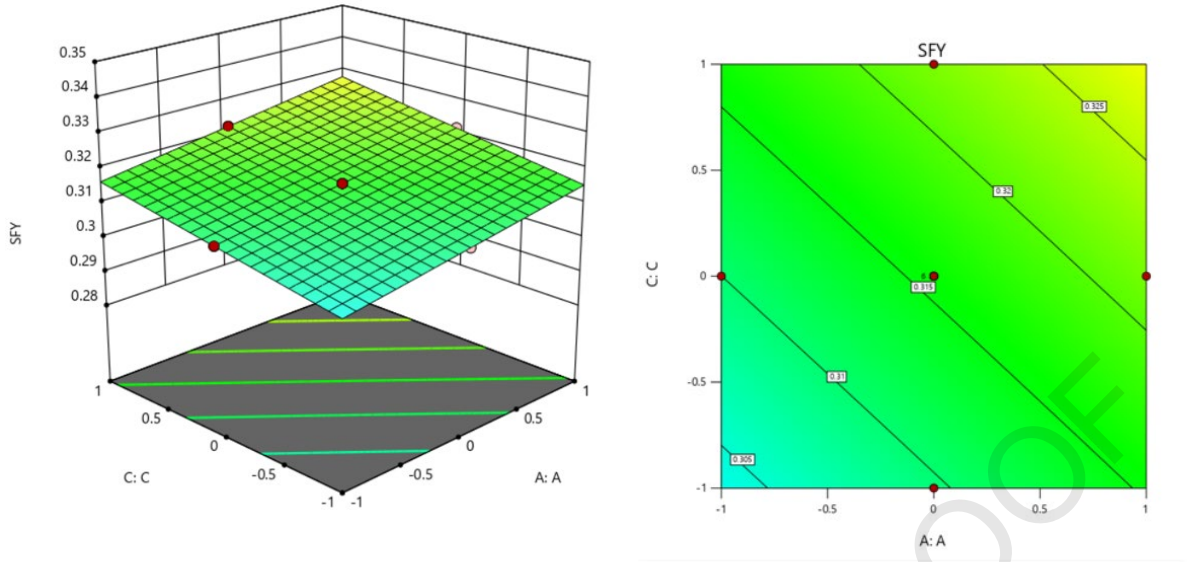

Figure 9 (b): Plots of A and C with response (skin friction in *y*-direction)

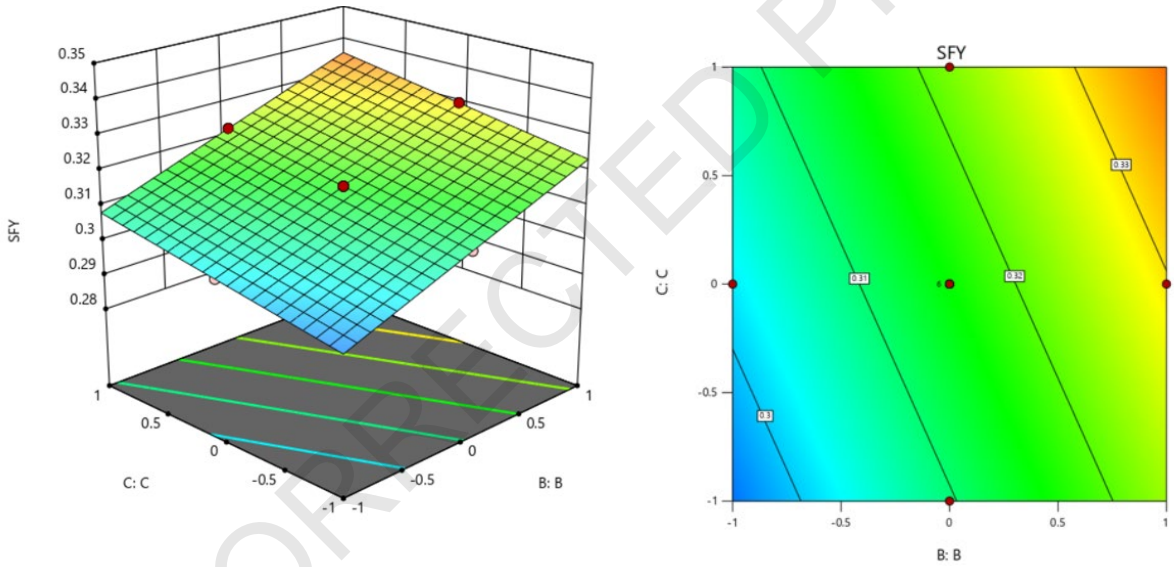

Figure 9 (c): Plots of C and B with response (skin friction in *y*-direction)

Figures 10 (a), (b), and (c) illustrate the relation between the coded parameters *A, B*, and *C* with the heat transfer rate (HT). These plots summarise that the heat transfer rate is maximised when parameters *A, B*, and *C* reach their maximum levels simultaneously. It can be observed that rapid improvement of HT is achieved with the increase of B, followed by *A* and *C*. Therefore, the heat transfer rate can be enhanced by augmenting the nanoparticle volume fraction of Cu, TiO_2, and Al_2O_3. However, the most notable enhancement is achieved with Cu nanoparticles, followed by Al_2O_3 and TiO_2 nanoparticles.

Further optimisation of HT can be analysed through the optimiser technique. With a desirability of 99.93%, $\mathrm{Re}_x^{-1/2}\, Nu_x$, representing the heat transfer rate, can achieve a maximum value of 0.442152 when parameters *A, B,* and *C* are all at their maximum levels (Table 10). This finding implies that the ternary hybrid nanofluid in the present model supports the notion that it could significantly enhance the heat-transfer performance in the fluid-flow system. The

RSM, coupled with the optimiser approach, has facilitated the identification of the optimal nanoparticle volume fraction combination that maximises the heat transfer rate, thereby demonstrating the potential of ternary hybrid nanofluids in improving thermal management and heat transfer efficiency.

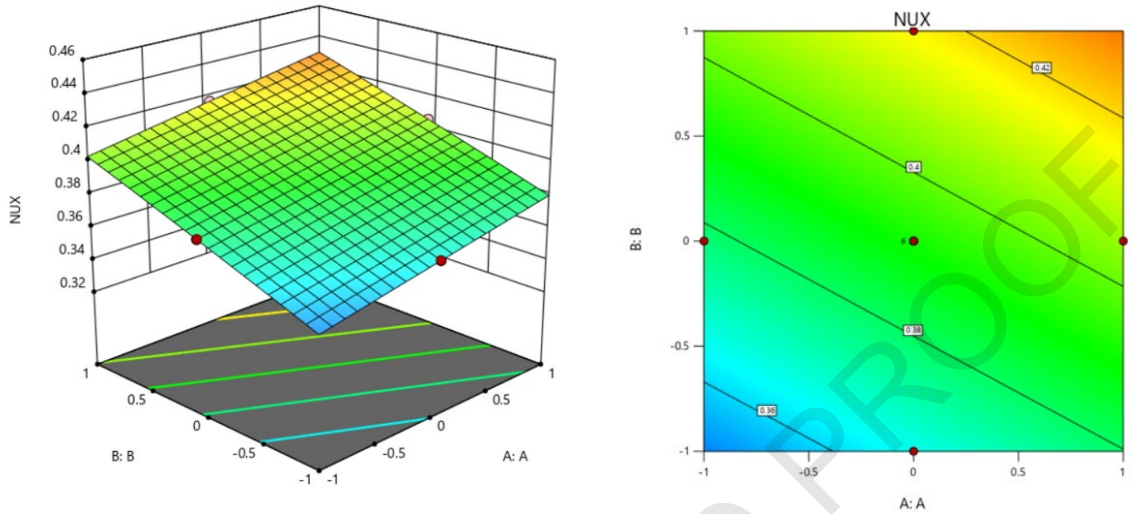

Figure 10 (a): Plots of *A* and *B* with response (heat transfer rate)

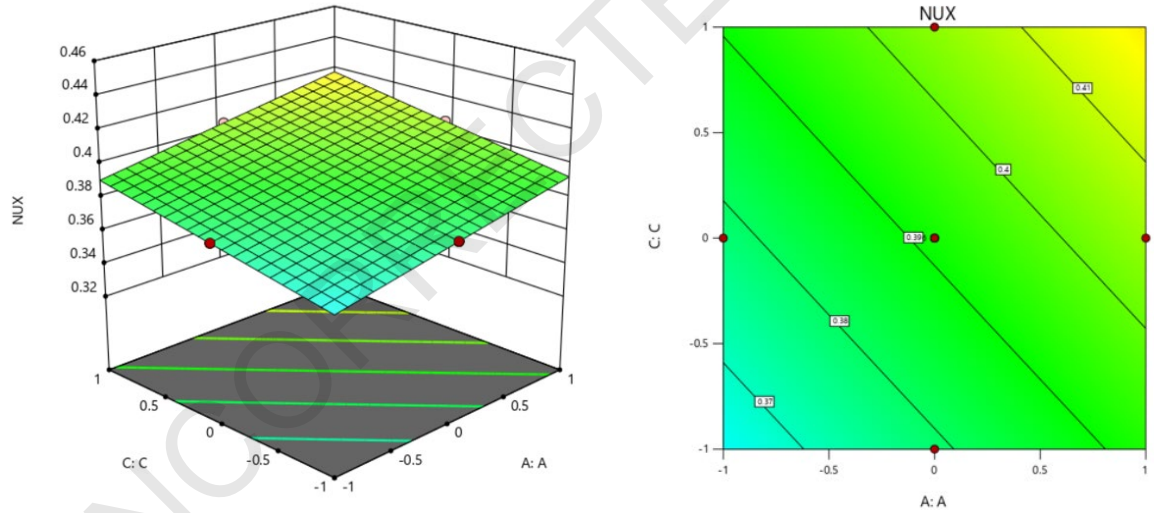

Figure 10 (b): Plots of *A* and *C* with response (heat transfer rate)

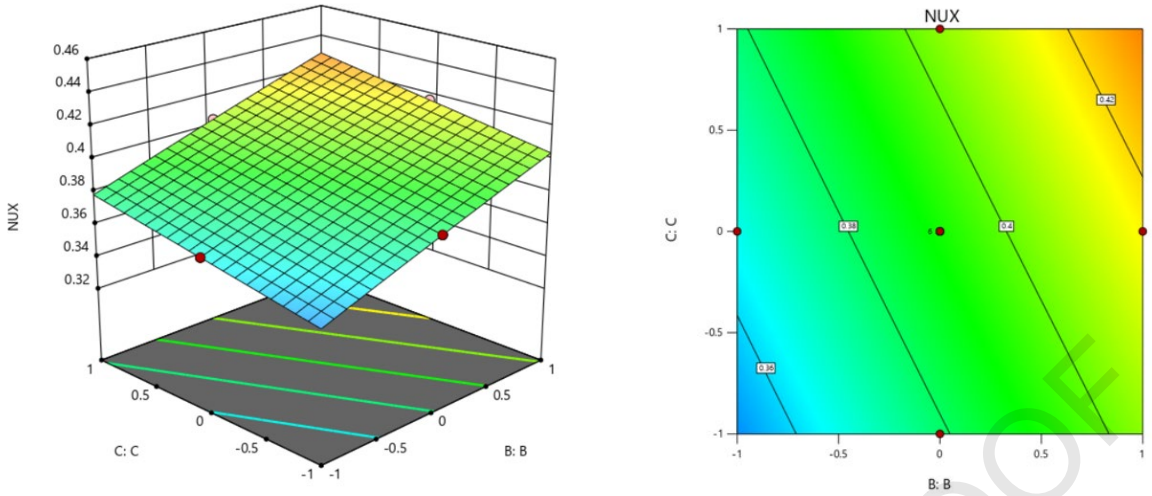

Figure 10 (c): Plots of *C* and *B* with response (heat-transfer rate)

Table 10: Optimisation: Response fit and desirability for heat transfer response

A	*B*	*C*	Response Fit	Composite Desirability
1	1	1	0.442152	0.999319

Conclusion

The three-dimensional model of rotating ternary hybrid nanofluid flow with opposing mixed convection past a vertical flat plate has been formulated and solved in this study. The formulated model is transformed into ordinary differential equations using appropriate similarity transformations. Both numerical and statistical analyses are conducted to examine the effects of the pertinent parameters on the physical quantities of interest. The key findings are as follows:

1. For the case of flow near the boundary,
   - the increase of opposing mixed convection parameter in magnitude has reduced $f'(\eta)$ but works in reverse for $g'(\eta)$, and $\theta(\eta)$.
   - the increase of rotating parameter has increased $f'(\eta)$ but produces an opposite effect for $g'(\eta)$, and $\theta(\eta)$.
2. The increase in nanoparticle volume fraction, notably Cu, significantly reduces skin friction in the *x*-direction, with TiO_2 and Al_2O_3 nanoparticles exhibit similar but less pronounced effects. However, the opposite effect is shown for the case of skin friction in *y*-direction.
3. Increasing the volume fraction of nanoparticles, particularly Cu, can significantly enhance the rate of heat transfer, with Cu nanoparticles demonstrating the greatest enhancement, followed by Al_2O_3 and TiO_2 nanoparticles.

It should be noted that the present findings are based on the assumptions underlying the proposed mathematical model and are valid only within the parameter's ranges considered in this study. The results are obtained under steady-state conditions using a boundary-layer approximation and a specific thermophysical properties. Therefore, further investigations may

be conducted by extending the analysis to wider parameter ranges, alternative hybrid nanofluid combinations, unsteady flow conditions, or by incorporating additional physical effects to enhance the applicability of the model.

Authors' Contributions

Nur Syahirah Wahid: Investigation, Methodology, Formal analysis, Writing — Review and Editing; Rusya Iryanti: Writing — Review and Editing; Nurul Izzah Khalid: Methodology, Software; Mohd Shafie Mustafa: Methodology, Software; Norihan Md Arifin: Supervision; Najiyah Safwa Khashi'ie: Software, Validation; Ioan Pop: Conceptualisation, Writing— Original draft preparation.

Acknowledgements

The authors would like to express their appreciation to Universiti Putra Malaysia for the financial support provided through the Putra Grant (GP-IPM 9787700).

Conflict of Interest Statement

The authors declare that there are no conflicts of interest.

References

[1] Adun, H., Kavaz, D., & Dagbasi, M. (2021). Review of ternary hybrid nanofluid: Synthesis, stability, thermophysical properties, heat transfer applications, and environmental effects. *Journal of Cleaner Production*, *328*, Article 129525. https://doi.org/10.1016/j.jclepro.2021.129525

[2] Alharbi, A. A. (2024). Thermal analysis of heat transport in a slip flow of ternary hybrid nanofluid with suction upon a stretching/shrinking sheet. *Case Studies in Thermal Engineering*, *54*, Article 103965. https://doi.org/10.1016/j.csite.2023.103965

[3] Asghar, A., Vrinceanu, N., Yuan Ying, T., Ali Lund, L., Shah, Z., & Tirth, V. (2023). Dual solutions of convective rotating flow of three-dimensional hybrid nanofluid across the linear stretching/shrinking sheet. *Alexandria Engineering Journal*, *75*, 297–312. https://doi.org/10.1016/j.aej.2023.05.089

[4] Devi, S. U., & Devi, S. A. (2017). Heat transfer enhancement of Cu-Al2O3/water hybrid nanofluid flow over a stretching sheet. *Journal of the Nigerian Mathematical Society*, *36*, 419–433.

[5] Hussain, Z., Aljuaydi, F., Ayaz, M., & Islam, S. (2024). Enhancing thermal efficiency in MHD kerosene oil-based ternary hybrid nanofluid flow over a stretching sheet with convective boundary conditions. *Results in Engineering*, *22*, Article 102151. https://doi.org/10.1016/j.rineng.2024.102151

[6] Jamrus, F. N., Waini, I., Khan, U., & Ishak, A. (2024). Effects of magnetohydrodynamics and velocity slip on mixed convective flow of thermally stratified ternary hybrid

nanofluid over a stretching/shrinking sheet. *Case Studies in Thermal Engineering*, *55*, Article 104161. https://doi.org/10.1016/j.csite.2024.104161

[7] Jan, S. U., Khan, U., El-Rahman, M. A., Islam, S., Hassan, A. M., & Ullah, A. (2023). Effect of variable thermal conductivity of ternary hybrid nanofluids over a stretching sheet with convective boundary conditions and magnetic field. *Results in Engineering*, *20*, Article 101531. https://doi.org/10.1016/j.rineng.2023.101531

[8] Khan, J. A., Mustafa, M., Hayat, T., & Alsaedi, A. (2014). On three-dimensional flow and heat transfer over a non-linearly stretching sheet: Analytical and numerical solutions. *PLOS ONE*, *9*, Article e107287. https://doi.org/10.1371/journal.pone.0107287

[9] Khan, U., Naveen Kumar, R., Zaib, A., Prasannakumara, B. C., Ishak, A., Galal, A. M., & Punith Gowda, R. J. (2022). Time-dependent flow of water-based ternary hybrid nanoparticles over a radially contracting/expanding and rotating permeable stretching sphere. *Thermal Science and Engineering Progress*, *36*, Article 101521. https://doi.org/10.1016/j.tsep.2022.101521

[10] Khashi'ie, N. S., Arifin, N. M., Wahid, N. S., & Pop, I. (2023). Insight into unsteady separated stagnation point flow of hybrid nanofluids subjected to an electro-magnetohydrodynamics Riga plate. *Magnetochemistry*, *9*, Article 46. https://doi.org/10.3390/magnetochemistry9020046

[11] Kodi, R., Ravuri, M. R., Veeranna, V., Ijaz Khan, M., Abdullaev, S., & Tamam, N. (2023). Hall current and thermal radiation effects of 3D rotating hybrid nanofluid reactive flow via stretched plate with internal heat absorption. *Results in Physics*, *53*, Article 106915. https://doi.org/10.1016/j.rinp.2023.106915

[12] Mahanthesh, B., Thriveni, K., Rana, P., & Muhammad, T. (2021). Radiative heat transfer of nanomaterial on a convectively heated circular tube with activation energy and nanoparticle aggregation kinematic effects. *International Communications in Heat and Mass Transfer*, *127*, Article 105568. https://doi.org/10.1016/j.icheatmasstransfer.2021.105568

[13] Mahmood, Z., Ahammad, N. A., Alhazmi, S. E., Khan, U., & Bani-Fwaz, M. Z. (2022). Ternary hybrid nanofluid near a stretching/shrinking sheet with heat generation/absorption and velocity slip on unsteady stagnation point flow. *International Journal of Modern Physics B*, *36*, Article 2250209. https://doi.org/10.1142/S0217979222502095

[14] Manjunatha, S., Puneeth, V., Gireesha, B. J., & Chamkha, A. J. (2022). Theoretical study of convective heat transfer in ternary nanofluid flowing past a stretching sheet. *Journal of Applied and Computational Mechanics*, *8*, 1279–1286. https://doi.org/10.22055/jacm.2021.37698.3067

[15] Mohana Ramana, R., Maheswari, C., Shaw, S. M., Dharmaiah, G., Fernandez-Gamiz, U., & Noeiaghdam, S. (2024). Numerical investigation of 3-D rotating hybrid nanofluid Forchheimer flow with radiation absorption over a stretching sheet. *Results in Engineering*, *22*, Article 102019. https://doi.org/10.1016/j.rineng.2024.102019

[16] Oztop, H. F., & Abu-Nada, E. (2008). Numerical study of natural convection in partially heated rectangular enclosures filled with nanofluids. *International Journal of Heat and Fluid Flow*, *29*, 1326–1336. https://doi.org/10.1016/j.ijheatfluidflow.2008.04.009

[17] Priyadharshini, P., Archana, M. V., Shah, N. A., & Alshehri, M. H. (2023). Ternary hybrid nanofluid flow emerging on a symmetrically stretching sheet optimization with machine learning prediction scheme. *Symmetry*, *15*, Article 1225. https://doi.org/10.3390/sym15061225

[18] Rajeswari, V., & Nath, G. (1992). Unsteady flow over a stretching surface in a rotating fluid. *International Journal of Engineering Science*, *30*, 747–756. https://doi.org/10.1016/0020-7225(92)90104-O

[19] Shanmugapriya, M., Sundareswaran, R., Senthil Kumar, P., & Rangasamy, G. (2022). Impact of nanoparticle shape in enhancing heat transfer of magnetized ternary hybrid nanofluid. *Sustainable Energy Technologies and Assessments*, *53*, Article 102700. https://doi.org/10.1016/j.seta.2022.102700

[20] Wahid, N. S., Arifin, N. M., Yahaya, R. I., Khashi'ie, N. S., & Pop, I. (2024). Impact of suction and thermal radiation on unsteady ternary hybrid nanofluid flow over a biaxial shrinking sheet. *Alexandria Engineering Journal*, *96*, 132–141. https://doi.org/10.1016/j.aej.2024.03.079

[21] Yacob, N. A., Dzulkifli, N. F., Salleh, S. N. A., Ishak, A., & Pop, I. (2021). Rotating flow in a nanofluid with CNT nanoparticles over a stretching/shrinking surface. *Mathematics*, *10*, Article 7. https://doi.org/10.3390/math10010007

[22] Yahaya, R. I., Mustafa, M. S., Md Arifin, N., Md Ali, F., & Mohamed Isa, S. S. P. (2024). Response surface methodology on MHD stagnation-point flow of ternary hybrid nanofluid over a permeable radially shrinking disk. *Numerical Heat Transfer, Part A: Applications*, 1–29. https://doi.org/10.1080/10407782.2024.2318000

[23] Yasir, M., Khan, M., Alqahtani, A. S., & Malik, M. Y. (2023). Mass transpiration effect on rotating flow of radiative hybrid nanofluid due to shrinking surface with irregular heat source/sink. *Case Studies in Thermal Engineering*, *44*, Article 102870. https://doi.org/10.1016/j.csite.2023.102870

[24] Zaki Ullah, A., Guo, X., Gul, T., Ali, I., Saeed, A., & Galal, A. M. (2023). Thin film flow of the ternary hybrid nanofluid over a rotating disk under the influence of magnetic field due to nonlinear convection. *Journal of Magnetism and Magnetic Materials*, *573*, Article 170673. https://doi.org/10.1016/j.jmmm.2023.170673